



1 Episodic subduction patches in the western North Pacific identified from BGC-Argo
2 float Data

3 Shuangling Chen¹, Mark L. Wells^{2,1}, Rui Xin Huang³, Huijie Xue², Jingyuan Xi¹, Fei
4 Chai^{1,2*}

5 ¹ State Key Laboratory of Satellite Ocean Environment Dynamics, Second Institute of
6 Oceanography, Ministry of Natural Resources, Hangzhou, China

7 ² School of Marine Sciences, University of Maine, Orono, ME, USA

8 ³ Woods Hole Oceanographic Institution, Woods Hole, MA, USA

9 *Corresponding author: Fei Chai (fchai@sio.org.cn)

10 Abstract

11 Subduction associated with mesoscale eddies is an important but difficult to observe
12 process that can efficiently export carbon and oxygen to the mesopelagic zone (100-
13 1000db). Using a novel BGC-Argo dataset covering the western North Pacific (20-
14 50°N, 120-180°E), we identified imprints of episodic subduction using anomalies in
15 dissolved oxygen and spicity, a water mass marker. These subduction patches were
16 present in 4.0% (288) of the total profiles (7,120) between 2008 and 2019, situated
17 mainly in the Kuroshio Extension region between March and August (70.6%). Unlike
18 eddy subduction processes observed at higher latitudes, roughly half (52%) of these
19 episodic events injected carbon- and oxygen-enriched waters below the annual
20 permanent thermocline depth (450 db), with >20% occurring deeper than 600 db.
21 Export rates within these subductions are estimated to be on the order of 85-159 mg C
22 m⁻² day⁻¹ and 175 to 417 mg O₂ m⁻² day⁻¹. These mesoscale events would markedly
23 increase carbon removal above that due to biological gravitational settling as well as
24 oxygen ventilation in the region, both helping to support the nutritional and metabolic
25 demands of mesopelagic organisms. Climate-driven patterns of increasing eddy kinetic
26 energies in this region imply that the magnitude of these processes will grow in the
27 future, meaning that these unexpectedly effective small-scale subduction processes
28 need to be better constrained in global climate and biogeochemical models.

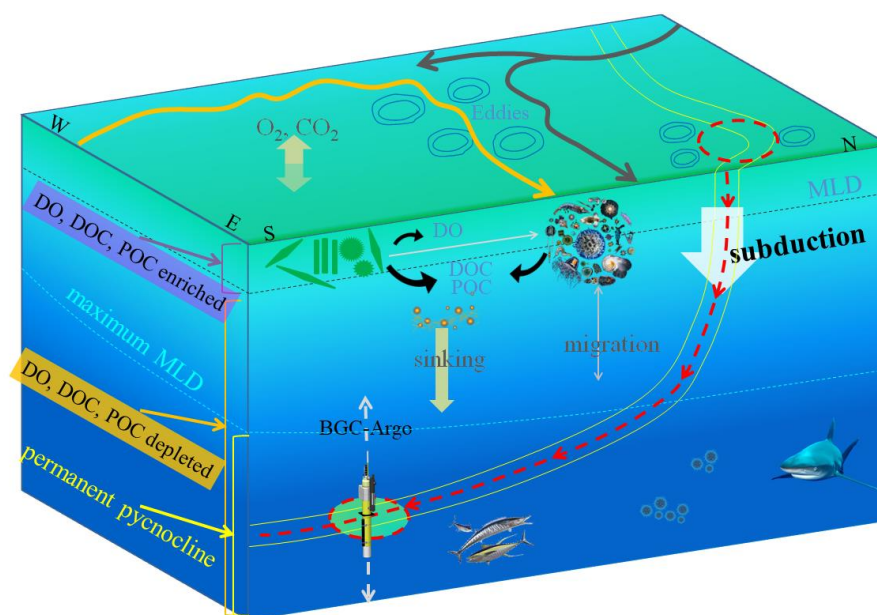
29 **Keywords:** dissolved oxygen; spicity; BGC-Argo; subduction; North Pacific

30 1. Introduction

31 Ocean subduction is the process of transporting water from the wind-mixed surface
32 layer into or below the permanent thermocline, resulting in the efficient injection of
33 heat, carbon and oxygen to the ocean interior (Fig. 1). Subduction therefore plays an
34 important role in regulating global climate and carbon cycles (Sabine et al., 2004; Qu
35 and Chen, 2009; Stukel et al., 2017 and 2018; Boyd et al., 2019; Martin et al., 2020).
36 Many studies focus on the subduction of mode waters driven by large-scale circulation,
37 and the seasonal cycle of the mixed layer dynamics (Williams, 2001; Qu et al., 2002;
38 Qiu et al., 2007; Koch-Larrouy et al., 2010; Kawakami et al., 2015; Nie et al., 2016).



39 But recent advances have highlighted the importance of small-scale (1-100 km)
40 dynamical processes on vertical transport and biogeochemistry in the upper ocean,
41 driven by mesoscale eddies and sub-mesoscale processes (Lévy et al., 2001; Xu et al.,
42 2014; Omand et al., 2015; McGillicuddy, 2016; Llorc et al., 2018; Resplandy et al.,
43 2019). Ocean general circulation models typically resolve the large-scale subduction of
44 mode waters (Koch-Larrouy et al., 2010) but cannot accurately capture small-scale,
45 short-term subduction processes because of their episodic characteristics (Xu et al.,
46 2014; Llorc et al., 2018).



47

48 **Fig. 1** An illustration of the Kuroshio and Oyashio extension region depicting the
49 different modes of carbon export below the maximum annual mixed layer depth; the
50 biological gravitational pump (sinking export, zooplankton migration) and subduction
51 in the region of the Kuroshio and its extension (yellow line) and Oyashio and its
52 extension (grey line). The subducted surface waters, apparently driven by mesoscale
53 eddy processes, travel along isopycnal surfaces transporting water containing high
54 dissolved oxygen (DO), dissolved organic carbon (DOC) and particulate organic
55 carbon (POC) into the mesopelagic zone (low DO, DOC, and POC). The green layer
56 represents the euphotic zone, and the blue layer below is the mesopelagic zone.

57 Subduction associated with mesoscale and sub-mesoscale dynamics has been observed
58 at higher latitudes in the North Atlantic (Omand et al., 2015) and Southern Oceans
59 (Llorc et al., 2018), and similar processes are shown to occur in Kuroshio Extension
60 (KE) region in the western subtropical Pacific. Shipboard sampling techniques have
61 been used there to identify small water parcels within the main thermocline having low
62 potential vorticity, elevated dissolved oxygen (DO), and anomalous salinity; signals



63 indicative of small-scale subduction (Yasuda et al., 1996; Okuda et al., 2001; Oka et
64 al., 2009). Analogous phenomena have been observed in mooring data from the region
65 (Nagano et al., 2016; Inoue et al., 2016a; Kouketsu et al., 2016; Zhu et al., 2021), and
66 more focused sampling of anticyclonic eddies with Argo floats (Zhang et al., 2015;
67 Inoue et al., 2016b) and SeaGliders (Hosoda et al., 2021) confirm the existence of
68 discrete subsurface water mass exchanges. These episodic features will contribute to
69 both ventilation of the mesopelagic zone as well as export of dissolved inorganic and
70 organic carbon from surface waters (i.e., the solubility pump (Sarmiento & Gruber,
71 2006), but their frequency, spatial extent and lifetimes remain unknown (Hosoda et al.,
72 2021).

73 Eddy-associated processes that generate vertical transport of productive and detrital
74 planktonic biomass into the mesopelagic zone affect not only carbon export but also
75 carbon sequestration time scales (i.e., time that carbon remains within the ocean
76 interior). In general, sequestration time scales are proportional to the depth of injection
77 but the more important factor is whether these injections extend below the annual
78 maximum mixed layer depth (MLD), or permanent pycnocline, which hinders its return
79 to the atmosphere (Boyd et al., 2019). Although eddy-subduction has the potential to
80 contribute significantly to global carbon export, evidence of the subsurface fate of
81 injected carbon has been indirect and patchy (Estapa et al., 2019), highlighting the
82 challenge of detecting and quantifying carbon export associated with mesoscale and
83 sub-mesoscale processes.

84 The uncertainty about the contribution of eddy subduction to carbon and oxygen
85 transport into the mesopelagic and deeper ocean interior has ramifications for both
86 biogeochemical and ecological processes (Fig. 1). The transport of freshly produced
87 particulate and dissolved organic carbon, along with oxygen, from surface waters to the
88 mesopelagic zone is critical for balancing upper ocean carbon budgets (Emerson, 2014)
89 and supporting the nutritional demands of mesopelagic organisms (Dall'Olmo et al.,
90 2016). The knowledge gap in these episodic processes is particularly evident in the mid-
91 latitude western North Pacific, where mesoscale eddies, recirculation gyres, fronts, and
92 jets are amplified under the influence of the Kuroshio and Oyashio currents and their
93 extensions (Nishikawa et al., 2010). Shoaling of the maximum annual MLD in this
94 region relative to higher latitudes (Cronin et al., 2013; Palevsky & Doney, 2018) has
95 the potential to increase carbon sequestration efficiency and oxygenation of the deep
96 mesopelagic zone (Bushinsky & Emerson, 2018).

97 Here we investigate small-scale subduction events in the western North Pacific region
98 over the past decade (2008-2019). These events were identified with a new algorithm
99 utilizing anomalies of apparent oxygen utilization (AOU; a proxy for dissolved and
100 particulate organic matter degradation) and potential spicity (π ; a characteristic water
101 mass marker) obtained from multiple biogeochemical Argo (BGC-Argo) datasets
102 (Claustre et al., 2020; Chai et al., 2020). These findings show the spatial and temporal
103 distributions of subduction patches reflecting episodic injection processes that
104 contribute to the missing fraction of carbon and oxygen export into the deep twilight

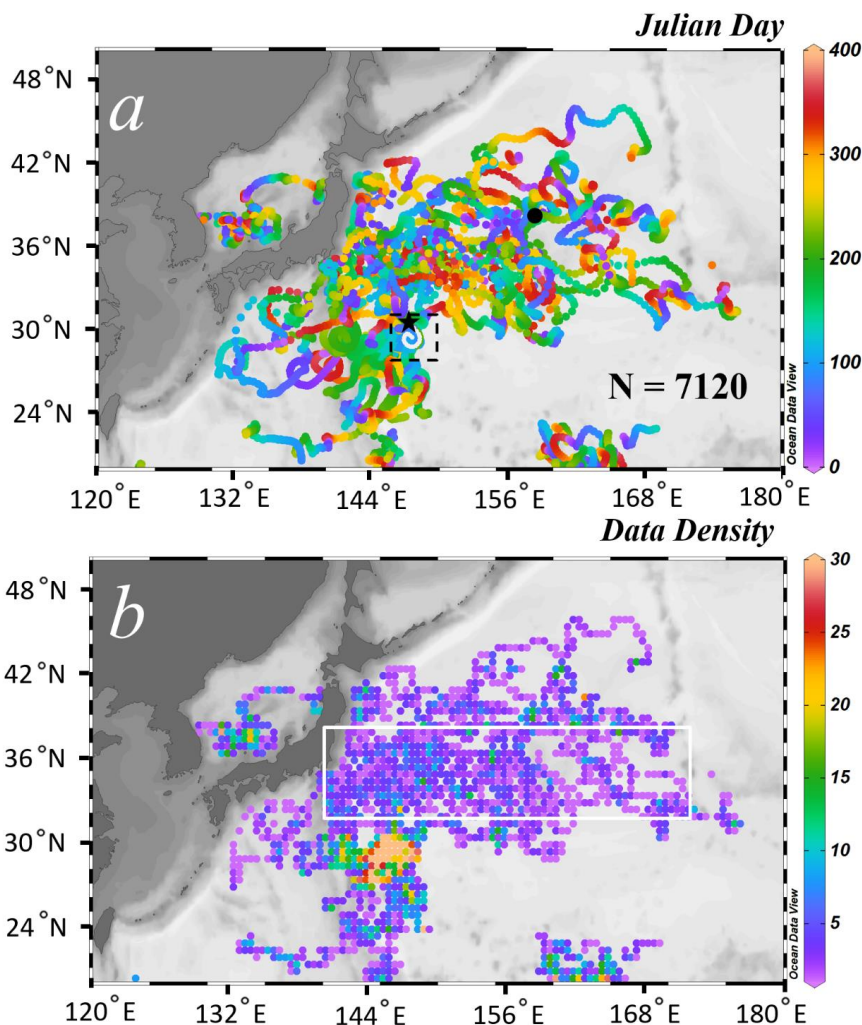


105 zone (Emerson, 2014; Martin et al., 2020), but also have the potential to become
106 increasingly significant under future climate scenarios.

107 **2. Data and Methods**

108 **2.1 Data**

109 After the standard data quality control, 7,120 profiles from 43 BGC-Argo floats in the
110 western North Pacific (20-50°N, 120-180°E) between 2008 and 2019 were selected (Fig.
111 2). All of these profiles contained measurements of temperature, salinity, pressure, and
112 dissolved oxygen (DO, $\mu\text{mol/kg}$). The upper 1000db of the ocean was sampled in each
113 profile and the typical profiling interval was between 5-10 days, with the floats parking
114 at 1000db depth in between. The typical vertical sampling frequency was every 5db,
115 10db, and 50db for depth intervals of 0-100db, 100-500db, and 500-1000db,
116 respectively. Some floats were set with daily profiling and higher vertical frequency
117 (e.g., every 2db) for specific purposes.



118

119 **Fig. 2** Horizontal distribution of the QCed BGC-Argo data profiles between 2008 and
120 2019 in the western North Pacific. The argo profiling tracks are color coded by Julian
121 day (a) and data density (number of available profiles) for each grid ($0.5^{\circ} \times 0.5^{\circ}$) (b). The
122 location of Station No. 234 from float MD5904034 is denoted by the black dot in (a)
123 (see Fig. 3); the white line in the dashed box represents the trajectory of float
124 MR2901556 between July 28th and August 18th in 2014, and the black star indicates
125 the beginning of the float trajectory during this period (see Fig. 4). The white box in (b)
126 denotes the region with strong energetic ocean processes.

127 All BGC-Argo variables were vertically smoothed with a 3-bin running average to
128 remove sharp noises or spikes (Llort et al., 2018). Two key variables, apparent oxygen



129 utilization (AOU) and potential spicity (π), were derived from the direct measurements.
130 Specifically, AOU is defined as the difference between saturated oxygen concentration
131 (O_{sat}) and DO, and O_{sat} is estimated from temperature and salinity (Garcia & Gordon,
132 1992). AOU is a proxy for water mass age which reflects the microbial respiration of
133 dissolved and particulate organic matter (Sarmiento & Gruber, 2006). Potential spicity
134 referenced to the surface pressure is calculated from pressure, temperature and salinity
135 following Huang et al. (2018), and it allows differentiating water masses with distinct
136 thermohaline properties but similar density. In addition, potential density (σ) referenced
137 to the surface pressure was derived from pressure, temperature and salinity based on
138 the thermodynamic equation (TEOS-10 (McDougall & Barker, 2011)); and MLD was
139 estimated based on a threshold (0.05 kg/m^3) of the difference in density from a near-
140 surface value (i.e., at 10db) (Brainerd & Gregg, 1995). All these derived variables were
141 calculated for each of the 7,120 profiles.

142 In addition to the BGC-Argo float data, satellite data of daily sea level anomalies (SLA)
143 and daily geostrophic velocity anomalies (u' and v') between 1993 and 2018 were also
144 processed. The geostrophic velocity anomalies were used to calculate the eddy kinetic
145 energy (EKE) as $\text{EKE} = \frac{1}{2} \sqrt{u'^2 + v'^2}$. These data were used to identify the spatial
146 relationship between surface mesoscale circulation and the float profiles.

147 2.2 Methods

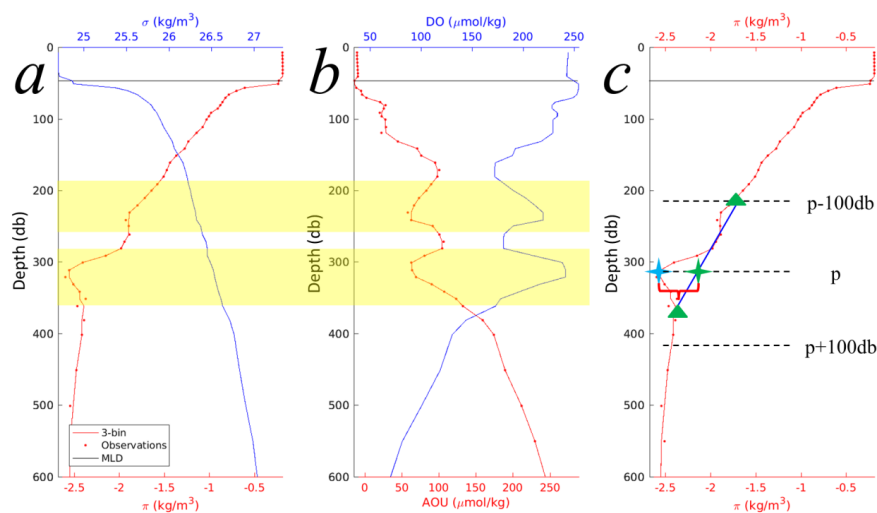
148 2.2.1 subduction detection

149 When a BGC-Argo float passes through a parcel of water injected from the mixed layer,
150 it captures coherent anomalous features in AOU and π distinct from the surrounding
151 waters (Fig. 1). These anomalies can be used to identify subduction patches that are
152 indicators of subduction events occurring in the vicinity (Omand et al., 2015; Llort et
153 al., 2018). Quantifying anomalies in AOU and π (denoted as Δ_{AOU} and Δ_{π}) requires
154 defining the reference values of AOU and π at the mean state of the profile without
155 subduction. Llort et al. (2018) used the 20-bin running averages of the profiles as the
156 references, however, we found that this approach could dampen the subduction signal
157 and thus miss subduction patches as well as misidentify other signals as subduction (see
158 Fig. S1). To avoid misreporting these anomalies, a revised detection method was
159 developed by trial and error, as shown in example profiles of AOU, π , DO and σ for
160 Station No. 234 of float MD5904034 (Fig. 3; see Fig. 2a for its sampling location). Two
161 subduction patches are visually apparent at $\sim 230\text{db}$ and $\sim 300\text{db}$ (yellow shades in Fig.
162 3a & 3b). The identification of the lower subduction patch at $\sim 300\text{db}$ from the spicity
163 profile is briefly described below and is illustrated in Fig. 3c:

- 164 1. Calculate the slopes (i.e., first-order derivative) for profiles of AOU and π
165 against depth;
- 166 2. Locate the peaks in AOU and π profiles (e.g., the blue star in Fig. 3c) based on
167 their slopes. Specifically, if at one sampling point the slope changes from
168 positive to negative when moving downwards, it is called a negative peak and



- 169 vice versa. Only the negative/positive peaks in π associated with a negative peak
170 in AOU are considered, as only negative AOU anomalies indicate potential
171 water transport from the surface mixed layer (Llort et al., 2018);
- 172 3. Locate the coherent peaks in both AOU and π , and mark their depths as the
173 targeted locations (represented by pressure, p) for potential subduction patches;
- 174 4. Calculate the peak $\Delta\pi$ at each targeted pressure. For the case of a negative
175 (positive) peak, identify the maximum (minimum) values of π within the depth
176 ranges of $[p-\Delta p, p]$ and $[p, p+\Delta p]$, respectively (green triangles in Fig. 3c), and
177 the depth interval $\Delta p=100\text{db}$ is chosen, considering the general vertical scale
178 (i.e., a few tens of meters) of the eddy-induced subduction features (Zhang et
179 al., 2015; Hosoda et al., 2021); the reference profile is defined by the straight
180 line in between. The anomaly $\Delta\pi$ (red bracket in Fig. 3c) is defined as the
181 difference between the reference profile and the original profile of π at pressure
182 p (green star in Fig. 3c);
- 183 5. Calculate Δ_{AOU} using the same method, independent of $\Delta\pi$;
- 184 6. The thresholds used to determine whether the signals meet the criteria of a
185 subduction patch or not were set to $-10\ \mu\text{mol}/\text{kg}$ for Δ_{AOU} and $\pm 0.05\ \text{kg}/\text{m}^3$ for
186 $\Delta\pi$ following Llort et al. (2018).



187

188 **Fig. 3** Vertical property distributions of profile No. 234 (on June 24th 2016) of float
189 MD5904034 (the black dot in Fig. 2a) demonstrate subduction patches observed by the
190 BGC-Argo floats. (a) The profiles of potential density (σ , blue line) and potential spicity
191 (π , red dotted line), (b) the profiles of DO (blue line) and AOU (red dotted line), and (c)
192 same spicity profile as in (a), which is used to demonstrate the steps to detect subduction
193 signals described in Methods. Note that the red dots in each panel represent the raw
194 field observations, the overlaid red curves are the 3-bin running averages to remove



195 sharp noises or spikes, and they are used to calculate the anomalies in AOU and π , and
196 the black line represents the MLD. The yellow shades in (a) and (b) highlight the
197 subduction features identified using the detection method in (c).

198 The refined algorithm presented here had improved performance for detecting
199 subduction patches in these BGC-Argo profile data than that used in previous studies
200 (Llort et al., 2018) (see Fig. S1). The main difference in our approach is in selecting the
201 frame of reference for identifying AOU and π anomalies from irregular features in
202 “typical” vertical profiles. We speculate that our refinements here may reveal more
203 episodic subduction patches in other datasets as well.

204 The sensitivity of the method to the interval of Δp (in step 4) was investigated by
205 varying Δp between 70db and 130db (see Table S1). For Δp of 100 ± 3 db (i.e., 97db,
206 98db, 99db, 101db, 102db, and 103db), less than 7 ($\leq 2\%$) subduction patches were
207 missed, and the resulted Δ_{AOU} and Δ_{π} show a RMSD of $\leq 3.8 \mu\text{mol/kg}$ ($\leq 8.3\%$) and \leq
208 0.03 kg/m^3 ($\leq 9.2\%$). More details are provided in Text S1. The sensitivity analysis
209 suggests the validity and robustness in the choice of Δp of 100db. After verifying that
210 this modified approach better captured subduction indicators in a subset of BGC-Argo
211 data from this region, the algorithm was applied to all profiles to identify the locations,
212 depths, time and strengths (i.e., Δ_{AOU} , Δ_{DO} and Δ_{π}) of the subduction patches.

213 2.2.2 Quantification of carbon and oxygen export

214 For all the subduction patches identified using the method developed above, we obtain
215 a first order estimate of carbon and oxygen export based on the AOU anomalies (Δ_{AOU})
216 and DO anomalies (Δ_{DO}) with the assumptions that: 1) the surface processes initiating
217 these subduction events generated similar levels of surface production (i.e., organic
218 carbon), and 2) the water parcels containing this organic carbon and DO are subducted
219 into the ocean's interior.

220 We begin by estimating the average carbon and oxygen inventories within the water
221 column based on the BGC-Argo profiles. We calculated AOU and DO inventories (per
222 m^2) through these features in two ways: integration of the anomaly above the estimated
223 baseline (Eqs. 1 & 2) and by using the anomaly peak height (Eqs. 3 & 4) (see Fig. 3c).
224 The integrated AOU inventory was converted to carbon using a Carbon:Oxygen (C:O)
225 remineralization ratio of 117:170 (Anderson and Sarmiento, 1994; Feely et al., 2004).

226 The equations for the integrated estimates for each profile are:

$$227 \quad \text{Carbon Inventory}_{\text{IA}} (\text{g C/m}^2) = \text{C:O} \times \sum_{z=p_1}^{z=p_2} \Delta \text{AOU}_z \quad (\text{Eq. 1})$$

$$228 \quad \text{Oxygen Inventory}_{\text{IA}} (\text{g O}_2/\text{m}^2) = \sum_{z=p_1}^{z=p_2} \Delta \text{DO}_z \quad (\text{Eq. 2})$$

229 where ΔAOU_z and ΔDO_z are the AOU and DO anomalies at depth z within the water
230 column of the subduction patch, and the integrated areas (IA) of AOU and DO
231 anomalies are converted from $\mu\text{mol kg}^{-1}$ to mg m^{-2} based on seawater density.



232 The inventories calculated using peak height (PH) approach are:

233
$$\text{Carbon Inventory}_{\text{PH}} (\text{g C/m}^2) = \text{C:O} \times \Delta_{\text{AOU_peak}} \times H \quad (\text{Eq. 3})$$

234
$$\text{Oxygen Inventory}_{\text{PH}} (\text{g O}_2/\text{m}^2) = \Delta_{\text{DO_peak}} \times H \quad (\text{Eq. 4})$$

235 where H is the thickness (i.e., vertical range from depth p1 to p2, in unit of m) of the
236 subduction patch and the $\Delta_{\text{AOU_peak}}$ and $\Delta_{\text{DO_peak}}$ are the maximum anomalous values of
237 AOU and DO converted to mg m^{-2} as above.

238 Converting these concentrations to carbon and oxygen export fluxes requires some
239 knowledge of subduction rates, which can vary exponentially from surface (~ 100 m/day)
240 to deep ocean (< 1 m/day). Rather than arbitrarily choosing a value in this range, we
241 take a more conservative approach by considering that it is reasonable to expect that
242 the subducted waters are renewed and dissipated on an annual scale. In other words, the
243 individual subduction processes have at most a 1-year lifetime, and therefore we
244 average the carbon and oxygen exports over 365 days (Eqs. 5-6).

245
$$\text{Carbon export} (\text{g C m}^{-2} \text{ d}^{-1}) = \text{Carbon inventory} / 365 \quad (\text{Eq. 5})$$

246
$$\text{Oxygen export} (\text{g O}_2 \text{ m}^{-2} \text{ d}^{-1}) = \text{Oxygen inventory} / 365 \quad (\text{Eq. 6})$$

247 using the inventories derived from Eqs. 1-4.

248 3. Results and Discussion

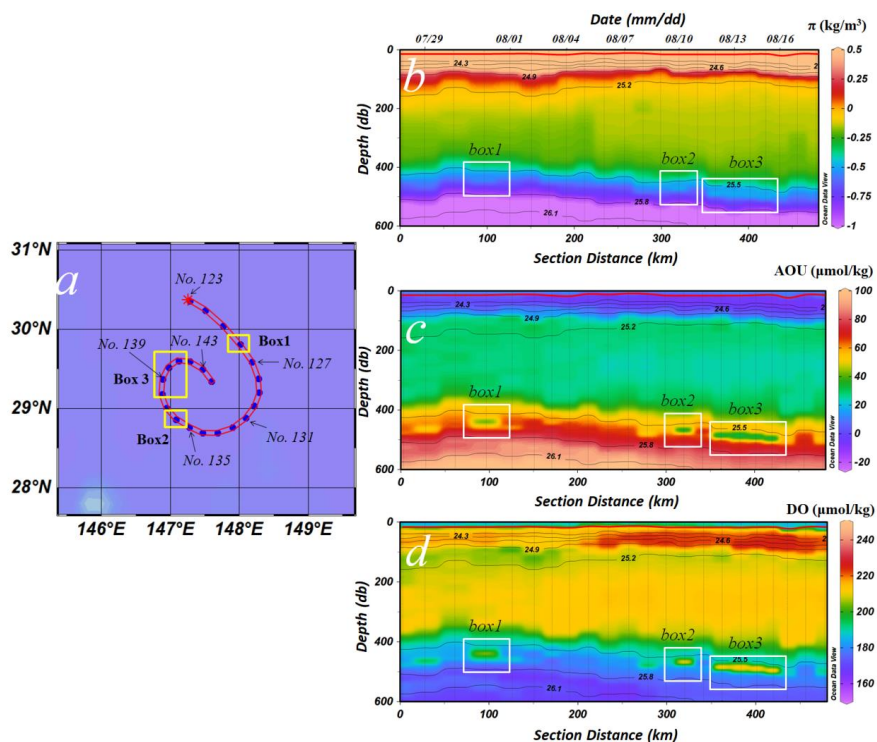
249 3.1 Case study: Detecting subduction in BGC-Argo datasets

250 Subduction associated with eddy pumping is a recognized important contributor to the
251 transfer of carbon and other materials from the surface euphotic layer to the ocean
252 interior (McGillicuddy, 2016; Bord et al., 2019), but investigating the spatial
253 distributions, physical dynamics, and biogeochemical consequences of these episodic
254 small-scale processes is difficult. The BGC-Argo program provides an exceptional data
255 resource for this purpose (Claustre et al., 2020; Chai et al., 2020), but detecting
256 subduction signals where differences among water masses are small is challenging.

257 Subduction below the seasonal and permanent pycnoclines can be identified in vertical
258 profiles by anomaly matrices of temperature, salinity, and dissolved oxygen (DO).
259 Examples of these events are illustrated in time-series from the BGC-Argo profiling
260 float (MR2901556), positioned on the southern perimeter of the Kuroshio Extension
261 region between July 28th and Aug. 18th 2014 (Fig. 4). Here, intermittent patches of
262 elevated spicity (π), lower AOU, and greater dissolved oxygen are visible in the upper
263 600 db (Boxes 1-3, Fig. 4). Potential spicity (π), a parameter dependent on pressure,
264 temperature and salinity (Huang et al., 2018), is a sensitive indicator of water mass
265 differences. AOU is the difference between the measured dissolved oxygen
266 concentration and its equilibrium saturation concentration in water with the same
267 physical and chemical properties. It reflects the degree of progressive microbial



268 decomposition of organic matter since the water was last at the surface in contact with
269 the atmosphere (Garcia & Gordon, 1992; Sarmiento & Gruber, 2006). Despite this
270 oxygen consumption, these injected waters retain excess net oxygen concentrations
271 relative to the surrounding mesopelagic zone (Fig. 4d).



272

273 **Fig. 4** Trajectory of float MR2901556 between July 28th 2014 (Station No. 123) and
274 August 18th, 2014 (Station No. 144) and its time series of π (b) AOU (c) and DO (d).
275 Vertical lines in (b), (c) and (d) represent the Bio-Argo profiles, and the section distance
276 along the X-axis is the path distance from Station No. 123 (the red star in (a)). The three
277 boxes (box1, box2, and box3) in panels (b,c,d) outline the coherent anomalous features
278 in π , AOU and DO, which were identified as subduction patches following the detection
279 procedure in Section 2.2.1. The red lines in panels (b,c,d) indicate the MLD, and the
280 horizontal black lines are the isopycnals. Anomalies of magnitude less than $-10 \mu\text{mol/kg}$
281 for Δ_{AOU} and $\pm 0.05 \text{ kg/m}^3$ for Δ_{π} (e.g., at section distances of $\sim 25\text{km}$, 125km , 175km ,
282 275km and 475km) were below our conservative thresholds for identifying intrusions
283 ($-10 \mu\text{mol/kg}$ for Δ_{AOU} and $\pm 0.05 \text{ kg/m}^3$ for Δ_{π}).

284 Llort et al. (2018) successfully identified eddy subduction in BGC-Argo data from the
285 Southern Ocean using anomalies in spiciness (Flament, 2002; Huang, 2011; McDougall
286 & Krzysik, 2015), a parameter derived from a different function of pressure,
287 temperature, and salinity than potential spicity (Huang et al., 2018). However, we found

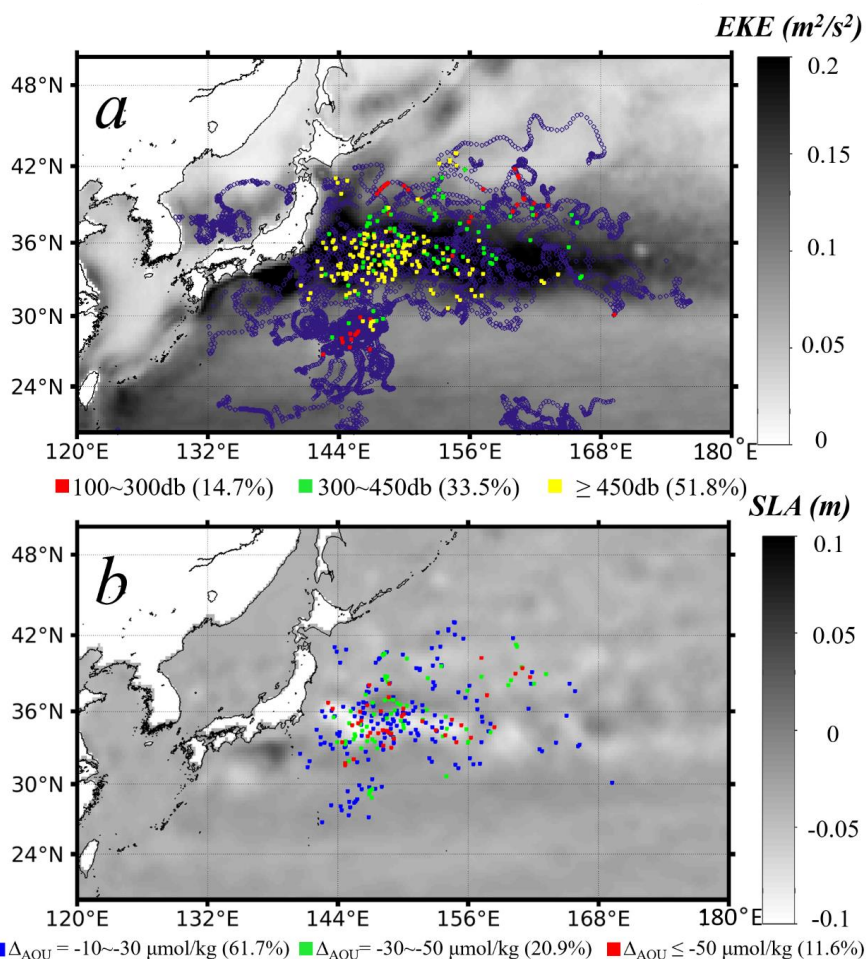


288 that spiciness frequently missed signs of subduction while misidentifying other signals
289 as subduction, and the 20-bin method used by Llort et al. (2018) significantly dampened
290 the subduction signals in our data. Potential spicity (π) (Huang et al., 2018), on the other
291 hand, greatly improves the ability to distinguish among similar water masses due to its
292 orthogonal coordination with density; a feature that spiciness lacks. This added
293 sensitivity revealed substantially more signals of subduction in these BGC-Argo data
294 than had been previously recognized. The modified algorithm based on peak detection
295 here shows better capabilities in capturing and quantifying the subduction signals (see
296 Methods, Fig. S1).

297 The ephemeral nature of the discrete anomalous π and AOU signals, highlighted in
298 boxes 1-3 in the example time series (Fig. 4a, b, c, and d; July 31st, Aug 10th, and August
299 12th to 15th) indicates that they stemmed from distinct subduction events,
300 opportunistically captured by this BGC-Argo float. The first two anomalies (July and
301 early August) each appeared in only a single profile, perhaps indicating a limited spatial
302 scale of these subduction events. In contrast, the mid-August anomaly persisted over 4
303 consecutive profiles, suggesting a more sustained, or a larger spatial subduction event.

304 **3.2 Spatial and temporal distributions of subduction**

305 We used our modified peak detection algorithm with the π and AOU data and applied
306 it to all 7,120 BGC-Argo profiles (2008-2019) in the western North Pacific (Fig. 5).
307 The modified algorithm resolved 335 subduction patches, spread over an unexpectedly
308 large area in the western North Pacific. Overall, subduction patches were identified in
309 288 profiles (4.0%) (some profiles have multiple patches at different depths), with
310 approximately 83% of these being concentrated in the Kuroshio-Oyashio extension
311 region (Fig. 5a). High (>10 cm) climatologic sea level anomalies (SLA) and the
312 corresponding distribution of Eddy Kinetic Energy (EKE) are evidence of the strong
313 energetic ocean processes in this region (Fig. 5). By contrast, far fewer subduction
314 patches were identified in the less energetic region to the south of 29°N despite a higher
315 BGC Argo sampling density (Fig. 2b), consistent with eddy-related processes being
316 important for driving these subduction events. Even so, the true frequency of these
317 events across the entire region is certain to have been under-sampled given their small
318 scales relative to the dispersed BGC-Argo float positions.



319

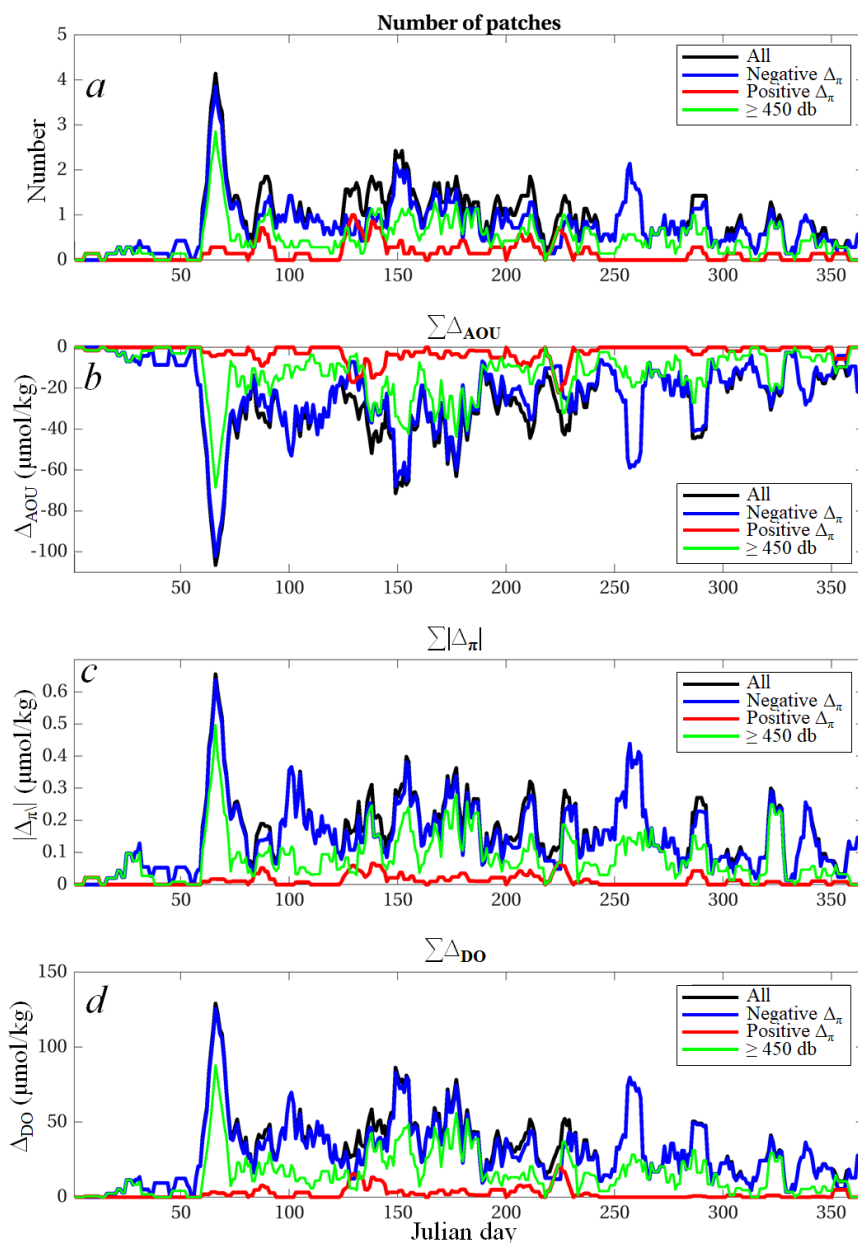
320 **Fig. 5** Horizontal distribution of the BGC-Argo data profiles associated with subduction
321 patches (a and b) between 2008 and 2019 in the western North Pacific. The profiles
322 with detected subduction patches are color coded by different intervals of depths of the
323 subduction patches (a) and AOU anomalies (b), with percentages of detected patches
324 in each interval annotated. The grey-scale background maps in (a) and (b) are the annual
325 mean EKE and SLA climatologies, and the purple background data in (a) represent all
326 the analyzed profiles as shown in Fig. 2a.

327 Discrete signals of subduction were detected throughout the mesopelagic depth range
328 (~100-1000db), with the majority detected below 300db (green and yellow dots in Fig.
329 5a). The deepest penetrations (≥ 450 db) occurred largely in areas experiencing the
330 highest EKE while the shallowest (100-300 db) were largely restricted to areas with
331 lower EKE (Fig. 5a). Roughly half (52%) of the detected subduction signals were
332 within or below the permanent pycnocline (450 db) in this region of the western North



333 Pacific (Cronin et al., 2013; Palevsky & Doney, 2018; Feucher et al., 2019), while 22%
334 penetrated far deeper (up to 800 db; Table S2 in supplemental materials).

335 There was a distinct seasonality in subduction, with most (~70%) signals being
336 observed between March (the maximum) and August (Figs. 6 & S2). Although only
337 8.3% of the total profiles were obtained in March, they accounted for 17.3% of all
338 observed subduction patches (Fig. S2), consistent with observations of large-scale
339 subduction in this region during late winter (Qu et al., 2002; Qiu et al., 2007; Nishikawa
340 et al., 2010; Liu & Huang, 2012; Zhang et al., 2014; Xu et al., 2014). The March to
341 August time frame also coincides with the onset and establishment of warming-induced
342 shoaling of the mixed layer depth, when winter-subducted waters are less likely to be
343 re-entrained into surface waters by winds (Dall'Olmo et al., 2016; Palevsky & Doney,
344 2018). In contrast, comparatively few (3.0%) of the subduction patches were detected
345 in January and February. Although specific timelines between the observed subduction
346 patches and their formation could not be determined, it is reasonable to anticipate that
347 more energetic winds and the accumulated strong heat loss during mid-winter
348 contributed to the peak in subduction signatures observed in March. The current BGC-
349 Argo profiling asset is not sufficient to study how those subduction patches change on
350 interannual scales.



351

352 **Fig. 6** Temporal distribution of the number of patches (a), integrated AOU anomaly (b),
353 integrated π anomaly (c), and integrated DO anomaly (d), by Julian day based on 7-
354 point smoothing. Spicity in subducted patches can be lower or higher than the
355 surrounding waters, resulting in negative $\Delta\pi$ (red lines) or positive $\Delta\pi$ (blue lines)
356 anomalies, respectively (see text in Section 3.4).

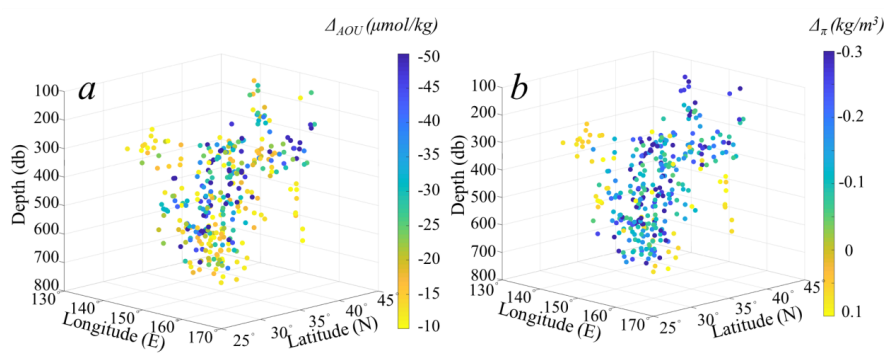


357 The Kuroshio-Oyashio extension zone lies between the subtropical and subpolar gyres
358 in the North Pacific, and it is a recognized hot-spot for water mass exchange via eddy
359 transport (Yasuda et al., 1996; Talley, 1997; Joyce et al., 2001; Zhang et al., 2014; Xu
360 et al., 2016) and substantial ocean-to-atmosphere heat flux (Jing et al., 2020). It is not
361 surprising then that the majority of subduction signals were observed in this region in
362 spite of less float coverage (Fig. 5). Large-scale circulation and seasonal variability in
363 the mixed layer depth here typically result in late winter subduction of subtropical mode
364 waters (Qiu et al., 2007; Oka et al., 2009; Oka & Qiu, 2012; Xu et al., 2014 & 2016),
365 and sharp horizontal density gradients can enhance strong vertical exchanges (Marshall
366 et al., 1993; Hurlburt et al., 1996; Liu et al., 2012; Ma et al., 2017). Rapid heat loss to
367 the winter-time cool, dry continental air masses flowing across the Kuroshio-Oyashio
368 extension erodes the seasonal thermocline to its maximum depth in February-March
369 (Cronin et al., 2013); the latter portion in which the subduction patches were most
370 frequently observed (Fig. 6).

371 Ascertaining the frequency and spatial extent of these lower-latitude episodic events
372 will be important for establishing their overall contribution to the transport of surface
373 waters into the mesopelagic zone, but this goal is challenged by the presently limited
374 distribution of BGC-Argo floats. It may be possible to obtain a first order estimate of
375 their frequency by linking the subduction signals here to surface-expressed indicators
376 of mesoscale circulation processes. Moreover, our findings suggest that spicity should
377 be adopted more generally in probing BGC-Argo datasets to improve our understanding
378 of the spatial and temporal distribution of subduction processes.

379 **3.3 Carbon and oxygen injections into the twilight zone**

380 Beyond being a water mass indicator, AOU is a proxy for cumulative net community
381 respiration and a sensitive indicator of carbon export in the upper mesopelagic zone
382 (Emerson et al., 2001; Pan et al., 2014; Catala et al., 2018; Bushinsky & Emerson, 2018).
383 This export comprises remineralized carbon as well as dissolved and slowly sinking
384 particulate organic matter carried by the subducting waters (Stukel et al., 2017). The
385 magnitude of AOU may be used as an indicator of the time since subduction, with the
386 first order assumption being that the larger scale processes initiating these subduction
387 events generated similar surface production. Values of Δ_{AOU} at the anomalous peak
388 depth ranged between -10 (the minimal threshold used) and -81 $\mu\text{mol/kg}$ (Fig. 7a). This
389 proxy was highly variable over the space-time domain, similar to the variations in Δ_{π}
390 (Fig. 7b). In general, 61.7% of the subduction patches had Δ_{AOU} in the range of -30 to
391 -10 $\mu\text{mol/kg}$ with the remainder having greater oxygen depletions (i.e., $\leq -30 \mu\text{mol/kg}$)
392 (Figs. 5b). Water masses subducted below 450db (i.e., the permanent pycnocline) had
393 an average AOU anomaly of $-25.7 \pm 15.3 \mu\text{mol/kg}$.



394

395 **Fig. 7** Vertical spatial distribution of the detected subduction patches in the western
396 North Pacific, color coded by the magnitudes of the subduction strengths in terms of
397 AOU anomaly (a) and π anomaly (b), respectively.

398 There was no clear relationship between the depth of subduction and AOU (Fig 7a),
399 suggesting either surface production was substantially different when these water
400 parcels were subducted, or that these signatures stem from non-systematic differences
401 in the time since subducted waters were last at the surface. Most subduction patches
402 with strong AOU anomalies were observed between March and August (particularly
403 March), after the seasonal mixed layer began to shoal, consistent with expected higher
404 levels of phytoplankton production. Only 0.6% of the total subduction patches had
405 Δ_{AOU} of $\leq -30 \mu\text{mol/kg}$ in January and February (Fig. S2b). The π anomalies show
406 similar variation patterns with months (peaked in March), with stronger Δ_{π} coupled
407 with stronger Δ_{AOU} (Fig. S2c).

408 Eddy associated pumping is one of several processes contributing to net global ocean
409 carbon export (McGillicuddy, 2016; Boyd et al., 2019), but its importance is generally
410 thought to be comparatively small because the relatively shallow penetration leads to
411 shorter carbon sequestration times (Lévy et al., 2001; Karleskind et al., 2011a & 2011b;
412 Omand et al., 2015; Nagai et al., 2015; Boyd et al., 2019). That is, much of the carbon
413 “exported” to the upper mesopelagic zone over spring and summer is returned to the
414 atmosphere by deep winter mixing. At higher latitudes, where eddy pumping has been
415 most studied, subduction must extend up to $> \sim 1000$ m to reach below the permanent
416 pycnocline (Palevsky & Doney, 2018; Boyd et al., 2019). However, the permanent
417 pycnocline in the western North Pacific is much shallower—on the order of ~ 400 db
418 (Qiu & Huang, 1995; Feucher et al., 2019)—and most of the observed subduction
419 signals here extended far below this depth (Table S2). Thus although the subduction
420 depths shown here are similar to those observed at higher latitudes, they represent much
421 longer carbon sequestration time scales than those previously associated with eddy
422 pumping (Boyd et al., 2019).

423 Similar small-scale subduction processes carry both particulate and dissolved organic
424 matter, and modeling suggests that this physical mechanism can be a major factor
425 influencing export of carbon from surface mixed layers to the upper mesopelagic zone



426 (McGillicuddy, 2016; Stukel et al., 2017 & 2018). In our case, the subduction patches
 427 contained on average negative AOU anomalies of $-27.6 \pm 16.4 \mu\text{mol/kg}$, with a
 428 maximum of $-81 \mu\text{mol/kg}$ in March (Figs. 6 & 7, Table 1); which are significantly
 429 stronger than that observed for eddy pumping processes in the Southern Ocean (Llort
 430 et al., 2018). This microbial oxygen consumption corresponds to remineralization of
 431 $\sim 19\text{-}56 \mu\text{mol C/kg}$. Carbon export rates within these subducting patches, based on the
 432 thickness of the subduction layer, the magnitude of AOU, and conservative estimates
 433 of advection rates, would be on the order of $85\text{-}218 \text{ mg C m}^{-2} \text{ day}^{-1}$ (Table 2); i.e., export
 434 rates similar in magnitude, but smaller in spatial scales, to that occurring in the North
 435 Atlantic spring bloom (Siegel et al., 2014). However, these values are likely an
 436 underestimate because only a portion of the organic carbon would have been degraded
 437 on these monthly time scales (Bushinsky & Emerson, 2018). Even so, the overall
 438 regional export associated with these events is difficult to estimate given that the
 439 subduction patches were only opportunistically captured by a comparatively wide
 440 separation of BGC-Argo profiles. The true frequency of these events is unknown.

441 The inferred injection dynamics observed here would partially offset the apparent
 442 imbalance between the biological gravitational pump and mesopelagic carbon budgets
 443 (Burd et al., 2010; Emerson, 2014) as well as the nutritional shortfalls for subsurface
 444 biota (Steinberg et al., 2008; Oka et al., 2009; Lacour et al., 2017). The intensity of
 445 these export events below the permanent pycnocline is remarkable, and they have not
 446 been adequately considered in biogeochemical models.

447 **Table 1** Summary of the subduction patches associated with positive and negative π
 448 anomalies; red numbers indicating statistics of the sum and mean based on absolute
 449 values of π anomalies.

Statistics	Number of patches	$\Delta_{\text{AOU}} (\mu\text{mol/kg})$		$\Delta_{\text{DO}} (\mu\text{mol/kg})$		$\Delta_{\pi} (\text{kg/m}^3)$	
		$\sum \Delta_{\text{AOU}}$	$\text{mean}(\Delta_{\text{AOU}})$	$\sum \Delta_{\text{DO}}$	$\text{mean}(\Delta_{\text{DO}})$	$\sum \Delta_{\pi}$	$\text{mean}(\Delta_{\pi})$
Total	335	-9248.43	-27.61	11560.79	34.51	58.57	0.17
$\Delta_{\pi} < 0$	279	-8303.75	-29.76	10743.84	38.51	-54.16	-0.19
$\Delta_{\pi} > 0$	56	-944.68	-16.87	816.95	14.59	4.41	0.08
Ratio ($\Delta_{\pi} < 0 / \Delta_{\pi} > 0$)	4.98	8.79	1.76	13.15	2.64	12.28	2.47

450 **Table 2** Statistics of the subduction-injected carbon and oxygen exports and export
 451 rates into the ocean's interior. See Section 2.2.2 for details on the calculation. Note that
 452 these statistics are based on the subduction patches identified, without considering their
 453 episodic characteristics and spatial and temporal inhomogeneity.

Method	Carbon Inventory (g C/m ²)	Oxygen Inventory (g O ₂ /m ²)	Carbon export (mg C/m ² /day)	Oxygen export (mg O ₂ /m ² /day)
Integrated Area	31.3±25.9	63.8±52.8	85.8±71.1	174.6±144.6
Peak Height	79.8±58.1	152.1±108.1	218.6±159.1	416.6±296.2

454



455 Global ocean inventories of oxygen have been decreasing, and current climate models
456 predict this trend is likely to accelerate over the next century (Oschlies et al., 2018).
457 However, these models suffer from considerable gaps in understanding, one of which
458 is the absence of small-scale transport processes such as the events captured here
459 (Oschlies et al., 2018). The average residual DO enrichment in the subduction patches,
460 defined as the difference in DO concentrations within and adjacent to the subducted
461 waters, was $34.5 \pm 19.8 \mu\text{mol O}_2/\text{kg}$, with levels as high as $\sim 88 \mu\text{mol O}_2/\text{kg}$ below 450
462 db during March (Table 1, Fig. 6). These differences reflected $\sim 20\%$ higher oxygen
463 concentrations than in the surrounding mesopelagic waters. Based on these residual
464 excess oxygen concentrations and very conservative estimates of advection rates, the
465 oxygen flux within these features would be on the order of $174\text{--}417 \text{ mg O}_2 \text{ m}^{-2} \text{ day}^{-1}$
466 (Table 2). These oxygen fluxes are $\sim 3\text{--}6$ times greater than the estimated mesopelagic
467 oxygen consumption rates in the highly productive Atlantic sector of the Southern
468 Ocean (Dehairs et al., 1997), and thus may represent a significant source of ventilation
469 to our study region.

470 Co-injection of oxygen below the permanent pycnocline by eddy pumping has not been
471 given close consideration in previous studies, largely because it is less relevant for high
472 latitude, oxygen-rich waters. However, weak ocean ventilation in the tropical and
473 subtropical mesopelagic zone is leading to declining oxygen concentrations
474 (Karstensen et al., 2008; Oschlies et al., 2018; Robinson, 2019) and expansion of
475 oxygen minimum zones in many regions of the oceans (Stramma et al., 2008; Breitburg
476 et al., 2018). These episodic, dispersed subduction events likely represent a significant
477 source of ventilation to help offset the de-oxygenation phenomenon, and to support the
478 expected climate-driven effects of increasing temperature on the metabolic oxygen
479 demand of mesopelagic organisms (Wohlers et al., 2009). Enriched oxygen supplies
480 into the mesopelagic zone also will influence remineralization rates of sinking
481 particulate organic carbon in the ocean's twilight zone (Buesseler et al., 2007; Steinberg
482 et al., 2008) affecting carbon sequestration time scales. Current global-scale
483 biogeochemical models currently are too coarse to capture the effect that these sub-
484 mesoscale processes may have on mesoscale oxygen variability (Takano et al., 2018),
485 or to account for this added oxygen supply.

486 **3.4 Surface forcing of subduction**

487 The AOU, DO and π anomalies were integrated within the study domain over the year
488 to assess the extent of subduction in the western North Pacific (Fig. 6, Table 1). π
489 anomalies were divided into negative or positive $\Delta\pi$ —i.e., π being greater or less than
490 that in surrounding waters—which can suggest their modes of formation. Negative $\Delta\pi$
491 would correspond with the subduction of colder waters, such as along the edges of
492 cyclonic eddies, while positive $\Delta\pi$ would be associated with the eddy pumping of
493 warmer core, anticyclonic eddies. The subduction patches were clearly dominated by
494 negative $\Delta\pi$, and more negative $\Delta\pi$ corresponded with much larger ΔAOU and ΔDO (Fig.
495 6), suggesting they were associated with cyclonic, cold core, upwelling-dominated
496 eddies that have higher oxygen solubilities, nutrient flux to the surface, and thus higher



497 plankton production. Conversely, the association of lower Δ_{AOU} and Δ_{DO} with positive
498 Δ_{π} would align with the lower oxygen solubility, nutrient flux and plankton production
499 expected for warmer core, downwelling anticyclonic eddies. Moreover, the majority
500 of deep intrusions had negative Δ_{π} (Fig. 6) consistent with colder waters following
501 deeper isoclines. In contrast, anticyclonic eddies would push warm, lower oxygen and
502 less biomass containing waters to shallower depths. These findings suggest that
503 tracking the activity of cyclonic eddies in regions with shoaling permanent pycnoclines
504 (Chelton et al., 2011; McGillicuddy, 2016) may be particularly important for
505 quantifying these deeper subduction processes.

506 The findings here indicate that eddy associated subduction is an important mechanism
507 driving carbon sequestration and oxygen enrichment below the permanent pycnocline
508 across the western subtropical Pacific region, particularly near the Kuroshio Extension
509 (KE). Moreover, the abundance of these discrete, small-scale subduction events almost
510 certainly is under-sampled in the BGC-Argo dataset. The frequency of this subduction
511 is expected to vary as the KE oscillates between two dynamic states—quasi-stable and
512 unstable—linked to the Pacific Decadal Oscillation (PDO) or North Pacific Gyre
513 Oscillation (NPGO) (Di Lorenzo et al., 2008). When quasi-stable, the KE jet shifts
514 north and generates less eddy activity than the unstable, highly meandering southward
515 KE jet, which reduces eastward transport and sharply increases eddy kinetic energy
516 (Qiu & Chen, 2010; Lin et al., 2014). Superimposed on these KE oscillations has been
517 an increase in the ratio of cyclonic to anticyclonic eddies associated with a climate-
518 driven intensification of tropical storms in the western Pacific and the multidecadal
519 trend of acceleration in Kuroshio flow (Zhang et al., 2020), suggesting that the
520 importance of eddy-associated subduction processes in this region has been increasing,
521 and may continue to increase in the future. This linkage needs to be considered in
522 designing future ocean observation programs and modeling of global biogeochemical
523 cycles to adequately capture the damping effects that eddy associated subduction may
524 exert on increasing atmospheric CO_2 and de-oxygenation in the tropical and subtropical
525 ocean.

526 4. Conclusion

527 Biogeochemical measurements obtained from the BGC-Argo float data provide new
528 insights into the small-scale vertical water mass exchange in the ocean. In particular,
529 spicity and AOU are key parameters in capturing the episodic subduction events and
530 their significance. Although these floats cannot capture the full pathways of subduction,
531 they provide the first-hand data on locations, depths, time, and strengths of episodic
532 subduction patches. Here we analyze float data in the western North Pacific and show
533 significant subduction export of dissolved oxygen and carbon to the mesopelagic zone
534 particularly below the permanent pycnocline; thus, the BGC-Argo data available over
535 the global oceans can be used to extend the current study to other oceanic regions. These
536 two factors—increased carbon export and re-oxygenation—would help to offset the
537 apparent budget imbalance between the biological gravitational pump and mesopelagic



538 carbon demand, and support the increasing metabolic oxygen demand of mesopelagic
539 organisms as ocean warming continues.

540 **Acknowledgements**

541 This work was supported by the National Key Research and Development Program of
542 China (2016YFC1401601), the National Natural Science Foundation of China (NSFC)
543 projects (41730536 and 41906159), the Scientific Research Fund of the Second
544 Institute of Oceanography, MNR (14283), and the Marine S&T Fund of Shandong
545 Province for Pilot National Laboratory for Marine Science and Technology (Qingdao)
546 (2018SDKJ0206).

547 **Author contributions**

548 S. C. was responsible for data processing and drafting the manuscript, R. X. H. and H.
549 X. took the lead in data analysis from the view of physical oceanography, M. L. W. and
550 F. C. contributed to the biogeochemical analysis, and F. C. designed and coordinated
551 the overall research project. All authors contributed to the ideas and writing of this
552 manuscript.

553 **Competing interests**

554 The authors declare no competing financial or research interests.

555 **Data availability**

556 The BGC-Argo data used in this study were collected and made freely available by the
557 International Argo Program and the national programs that contribute to it
558 (<http://www.argo.ucsd.edu>, <http://argo.jcommops.org>), archived in the Argo Global
559 Data Assembly Centre (<http://doi.org/10.17882/42182>), and quality-controlled and
560 made available by the China Argo Real-time Data Center (<http://www.argo.org.cn>).
561 The satellite SLA and geostrophic velocity data are from the Archiving, Validation and
562 Interpretation of Satellite Data in Oceanography (AVISO) and can be downloaded from
563 the Copernicus Marine Environment Monitoring Service
564 (<https://marine.copernicus.eu/>).

565 **References**

- 566 Boyd, P.W., Claustre, H., Levy, M., Siegel, D.A. and Weber, T., 2019. Multi-faceted
567 particle pumps drive carbon sequestration in the ocean. *Nature*, 568(7752), 327-335.
568 Brainerd, K. E., & Gregg, M. C., 1995. Surface mixed and mixing layer depths. *Deep*
569 *Sea Research Part I: Oceanographic Research Papers*, 42(9), 1521-1543.
570 Breitbart, D., Levin, L. A., Oschlies, A., Grégoire, M., Chavez, F. P., Conley, D. J., ...
571 & Jacinto, G. S., 2018. Declining oxygen in the global ocean and coastal waters.
572 *Science*, 359(6371), eaam7240.
573 Buesseler, K. O., Lamborg, C. H., Boyd, P. W., Lam, P. J., Trull, T. W., Bidigare, R.
574 R., ... & Honda, M., 2007. Revisiting Carbon Flux Through the Ocean's Twilight
575 Zone. *Science*, 316(5824), 567-570.



- 576 Burd, A. B., Hansell, D. A., Steinberg, D. K., Anderson, T. R., Arístegui, J., Baltar,
577 F., ... & Kadko, D. C., 2010. Assessing the apparent imbalance between
578 geochemical and biochemical indicators of meso-and bathypelagic biological
579 activity: What the@ \$#! is wrong with present calculations of carbon budgets?.
580 Deep Sea Research Part II: Topical Studies in Oceanography, 57(16), 1557-1571.
- 581 Bushinsky, S. M., & Emerson, S. R., 2018. Biological and physical controls on the
582 oxygen cycle in the Kuroshio Extension from an array of profiling floats. Deep
583 Sea Research Part I: Oceanographic Research Papers, 141, 51-70.
- 584 Catala, T. S., Martinez-Perez, A. M., Nieto-Cid, M., Alvarez, M., Otero, J., Emelianov,
585 M., Reche, I., Aristegui, J., & Alvarez-Salgado, X. A. (2018). Dissolved Organic
586 Matter (DOM) in the open Mediterranean Sea. I. Basin-wide distribution and
587 drivers of chromophoric DOM. Progress in Oceanography, 165, 35-51.
588 doi:10.1016/j.pocean.2018.05.002
- 589 Chai, F., Johnson, K. S., Claustre, H., Xing, X., Wang, Y., Boss, E., ... & Sutton, A.,
590 2020. Monitoring ocean biogeochemistry with autonomous platforms. Nature
591 Reviews Earth & Environment, 1, 315-326.
- 592 Chelton, D. B., Schlax, M. G., & Samelson, R. M., 2011. Global observations of
593 nonlinear mesoscale eddies. Progress in oceanography, 91(2), 167-216.
- 594 Claustre, H., Johnson, K.S. and Takeshita, Y., 2020. Observing the Global Ocean with
595 Biogeochemical-Argo. Annual review of marine science, 12, 11.1-11.26.
- 596 Cronin, M. F., Bond, N. A., Farrar, J. T., Ichikawa, H., Jayne, S. R., Kawai, Y., Konda,
597 M., Qiu, B., Rainville, L., & Tomita, H., 2013. Formation and erosion of the
598 seasonal thermocline in the Kuroshio Extension Recirculation Gyre. Deep-Sea
599 Research Part II-Topical Studies in Oceanography, 85, 62-74.
600 doi:10.1016/j.dsr2.2012.07.018
- 601 Dall'Olmo, G., Dingle, J., Polimene, L., Brewin, R.J. and Claustre, H., 2016. Substantial
602 energy input to the mesopelagic ecosystem from the seasonal mixed-layer pump.
603 Nature Geoscience, 9(11), 820-823.
- 604 Dehairs, F., Shopova, D., Ober, S., Veth, C. and Goeyens, L., 1997. Particulate barium
605 stocks and oxygen consumption in the Southern Ocean mesopelagic water column
606 during spring and early summer: relationship with export production. Deep Sea
607 Research Part II: Topical Studies in Oceanography, 44(1): 497-516.
- 608 Di Lorenzo, E., Schneider, N., Cobb, K. M., Franks, P. J. S., Chhak, K., Miller, A. J., ...
609 & Powell, T. M., 2008. North Pacific Gyre Oscillation links ocean climate and
610 ecosystem change. Geophysical Research Letters, 35(8).
- 611 Emerson, S., Mecking, S., & Abell, J., 2001. The biological pump in the subtropical
612 North Pacific Ocean: Nutrient sources, Redfield ratios, and recent changes. Global
613 biogeochemical cycles, 15(3), 535-554.
- 614 Emerson, S., 2014. Annual net community production and the biological carbon flux in
615 the ocean. Global Biogeochemical Cycles, 28(1), 14-28.
- 616 Estapa, M. L., Feen, M. L., & Breves, E., 2019. Direct observations of biological carbon
617 export from profiling floats in the subtropical North Atlantic. Global
618 Biogeochemical Cycles, 33(3), 282-300.



- 619 Feucher, C., Maze, G., & Mercier, H., 2019. Subtropical mode water and permanent
620 pycnocline properties in the world ocean. *Journal of Geophysical Research: Oceans*,
621 124(2), 1139-1154.
- 622 Flament, P., 2002. A state variable for characterizing water masses and their diffusive
623 stability: spiciness. *Progress in Oceanography*, 54(1-4), 493-501.
- 624 Garcia, H.E. and Gordon, L.I., 1992. Oxygen solubility in seawater: Better fitting
625 equations. *Limnology and oceanography*, 37(6), 1307-1312.
- 626 Hosoda, S., Inoue, R., Nonaka, M., Sasaki, H., Sasai, Y., & Hirano, M. (2021). Rapid
627 water parcel transport across the Kuroshio Extension in the lower thermocline
628 from dissolved oxygen measurements by Seaglider. *Progress in Earth and
629 Planetary Science*, 8(1), 1-19.
- 630 Huang, R. X., 2011. Defining the spicity. *Journal of Marine Research*, 69(4-5), 545-
631 559.
- 632 Huang, R.X., Yu, L.-S. and Zhou, S.-Q., 2018. Potential spicity defined by the least
633 square method, *Journal of Geophysical Research, Ocean*, 123, 7351-7365.
- 634 Hurlburt, H.E., Wallcraft, A.J., Schmitz Jr, W.J., Hogan, P.J. and Metzger, E.J., 1996.
635 Dynamics of the Kuroshio/Oyashio current system using eddy-resolving models of
636 the North Pacific Ocean. *Journal of Geophysical Research: Oceans*, 101(C1), 941-
637 976.
- 638 Inoue, R., Honda, M. C., Fujiki, T., Matsumoto, K., Kouketsu, S., Suga, T., & Saino,
639 T. (2016a). Western North Pacific integrated physical-biogeochemical ocean
640 observation experiment (INBOX): Part 2. Biogeochemical responses to eddies and
641 typhoons revealed from the S1 mooring and shipboard measurements. *Journal of
642 Marine Research*, 74(2), 71-99.
- 643 Inoue, R., Suga, T., Kouketsu, S., Kita, T., Hosoda, S., Kobayashi, T., ... & Kawano, T.
644 (2016b). Western north Pacific integrated physical-biogeochemical ocean
645 observation experiment (INBOX): part 1. Specifications and chronology of the S1-
646 INBOX floats. *Journal of Marine Research*, 74(2), 43-69.
- 647 Jing, Z., Wang, S., Wu, L., Chang, P., Zhang, Q., Sun, B., ... & Chen, Z. (2020).
648 Maintenance of mid-latitude oceanic fronts by mesoscale eddies. *Science advances*,
649 6(31), eaba7880.
- 650 Joyce, T. M., Yasuda, I., Hiroe, Y., Komatsu, K., Kawasaki, K., & Bahr, F., 2001.
651 Mixing in the meandering Kuroshio Extension and the formation of North Pacific
652 Intermediate Water. *Journal of Geophysical Research: Oceans*, 106(C3), 4397-4404.
- 653 Karleskind, P., Lévy, M., & Mémerly, L., 2011a. Subduction of carbon, nitrogen, and
654 oxygen in the northeast Atlantic. *Journal of Geophysical Research: Oceans*,
655 116(C2).
- 656 Karleskind, P., Lévy, M., & Mémerly, L., 2011b. Modifications of mode water
657 properties by sub-mesoscales in a bio-physical model of the Northeast Atlantic.
658 *Ocean Modelling*, 39(1-2), 47-60.
- 659 Karstensen, J., Stramma, L., & Visbeck, M., 2008. Oxygen minimum zones in the
660 eastern tropical Atlantic and Pacific oceans. *Progress in Oceanography*, 77(4), 331-
661 350.



- 662 Kawakami, Y., Sugimoto, S., and Suga, T., 2015. Inter-annual zonal shift of the
663 formation region of the lighter variety of the north pacific central mode water.
664 *Journal of Oceanography*, 72(2), 1-10.
- 665 Koch-Larrouy, A., Morrow, R., Penduff, T. and Juza, M., 2010. Origin and mechanism
666 of Subantarctic Mode Water formation and transformation in the Southern Indian
667 Ocean. *Ocean Dynamics*, 60(3), 563-583.
- 668 Kouketsu, S., Inoue, R., & Suga, T. (2016). Western North Pacific integrated physical-
669 biogeochemical ocean observation experiment (INBOX): part 3. Mesoscale
670 variability of dissolved oxygen concentrations observed by multiple floats during
671 S1-INBOX. *Journal of Marine Research*, 74(2), 101-131.
- 672 Lacour, L., Ardyna, M., Stec, K. F., Claustre, H., Prieur, L., Poteau, A., et al., 2017.
673 Unexpected winter phytoplankton blooms in the North Atlantic subpolar gyre.
674 *Nature Geoscience*, 10(11), 836-839.
- 675 Lévy, M., Klein, P. and Treguier, A.M., 2001. Impact of sub-mesoscale physics on
676 production and subduction of phytoplankton in an oligotrophic regime. *Journal of*
677 *Marine Research*, 59(4), 535-565.
- 678 Lin, P., Chai, F., Xue, H., & Xiu, P., 2014. Modulation of decadal oscillation on surface
679 chlorophyll in the Kuroshio Extension. *Journal of Geophysical Research: Oceans*,
680 119(1), 187-199.
- 681 Liu, L.L. and Huang, R.X., 2012. The global subduction/obduction rates: Their
682 interannual and decadal variability. *Journal of Climate*, 25(4), 1096-1115.
- 683 Liu, Y., Dong, C., Guan, Y., Chen, D., McWilliams, J. and Nencioli, F., 2012. Eddy
684 analysis in the subtropical zonal band of the North Pacific Ocean. *Deep Sea*
685 *Research Part I: Oceanographic Research Papers*, 68, 54-67.
- 686 Llorc, J., Langlais, C., Matear, R., Moreau, S., Lenton, A. and Strutton, P.G., 2018.
687 Evaluating Southern Ocean carbon eddy-pump from biogeochemical-Argo floats.
688 *Journal of Geophysical Research: Oceans*, 123(2), 971-984.
- 689 Ma, X., Chang, P., Saravanan, R., Montuoro, R., Nakamura, H., Wu, D., Lin, X. and
690 Wu, L., 2017. Importance of resolving Kuroshio front and eddy influence in
691 simulating the North Pacific storm track. *Journal of Climate*, 30(5), 1861-1880.
- 692 Marshall, J.C., Williams, R.G. and Nurser, A.G., 1993. Inferring the subduction rate
693 and period over the North Atlantic. *Journal of Physical Oceanography*, 23(7), 1315-
694 1329.
- 695 Martin, A., Boyd, P., Buesseler, K., Cetinic, I., Claustre, H., Giering, S., ... & Robinson,
696 C., 2020. The oceans' twilight zone must be studied now, before it is too late. *Nature*,
697 580, 26-28.
- 698 McDougall, T., & Barker, P., 2011. Getting started with TEOS-10 and the Gibbs
699 Seawater (GSW) oceanographic toolbox. SCOR/IAPSO, WG127, pp 28.
- 700 McDougall, T. J., & Krzysik, O. A., 2015. Spiciness. *Journal of Marine Research*, 73(5),
701 141-152.
- 702 McGillicuddy, D.J., 2016. Mechanisms of Physical-Biological-Biogeochemical
703 Interaction at the Oceanic Mesoscale. *Annual Review of Marine Science*, 8, 125-
704 159.



- 705 Nagai, T., Gruber, N., Frenzel, H., Lachkar, Z., McWilliams, J. C., & Plattner, G. K.,
706 2015. Dominant role of eddies and filaments in the offshore transport of carbon and
707 nutrients in the California Current system. *Journal of Geophysical Research:*
708 *Oceans*, 120(8), 5318-5341.
- 709 Nagano, A., Suga, T., Kawai, Y., Wakita, M., Uehara, K., & Taniguchi, K., 2016.
710 Ventilation revealed by the observation of dissolved oxygen concentration south of
711 the Kuroshio Extension during 2012–2013. *Journal of Oceanography*, 72(6), 837-
712 850.
- 713 Nie, X., Gao, S., Wang, F., & Qu, T., 2016. Subduction of north pacific tropical water
714 and its equatorward pathways as shown by a simulated passive tracer. *Journal of*
715 *Geophysical Research: Oceans*, 121.
- 716 Nishikawa, S., Tsujino, H., Sakamoto, K. and Nakano, H., 2010. Effects of mesoscale
717 eddies on subduction and distribution of subtropical mode water in an eddy-
718 resolving OGCM of the western North Pacific. *Journal of Physical Oceanography*,
719 40(8), 1748-1765.
- 720 Oka, E., Toyama, K. and Suga, T., 2009. Subduction of North Pacific central mode
721 water associated with subsurface mesoscale eddy. *Geophysical Research Letters*,
722 36(8), L08607.
- 723 Oka, E. and Qiu, B., 2012. Progress of North Pacific mode water research in the past
724 decade. *Journal of oceanography*, 68(1), 5-20.
- 725 Okuda, K., Yasuda, I., Hiroe, Y., & Shimizu, Y., 2001. Structure of subsurface intrusion
726 of the Oyashio water into the Kuroshio Extension and formation process of the
727 North Pacific Intermediate Water. *Journal of oceanography*, 57(2), 121-140.
- 728 Omand, M.M., D'Asaro, E.A., Lee, C.M., Perry, M.J., Briggs, N., Cetinić, I. and
729 Mahadevan, A., 2015. Eddy-driven subduction exports particulate organic carbon
730 from the spring bloom. *Science*, 348(6231), 222-225.
- 731 Oschlies, A., Brandt, P., Stramma, L., & Schmidtko, S., 2018. Drivers and mechanisms
732 of ocean deoxygenation. *Nature Geoscience*, 11(7), 467-473.
- 733 Palevsky, H. I., & Doney, S. C., 2018. How choice of depth horizon influences the
734 estimated spatial patterns and global magnitude of ocean carbon export flux.
735 *Geophysical Research Letters*, 45, 4171–4179. [https://doi.org/10.1029/
736 2017GL076498](https://doi.org/10.1029/2017GL076498)
- 737 Pan, X., Achterberg, E. P., Sanders, R., Poulton, A. J., Oliver, K. I., & Robinson, C.,
738 2014. Dissolved organic carbon and apparent oxygen utilization in the Atlantic
739 Ocean. *Deep Sea Research Part I: Oceanographic Research Papers*, 85, 80-87.
- 740 Qiu, B., & Huang, R. X., 1995. Ventilation of the North Atlantic and North Pacific:
741 subduction versus obduction. *Journal of Physical Oceanography*, 25(10), 2374-
742 2390.
- 743 Qiu, B., Chen, S. and Hacker, P., 2007. Effect of mesoscale eddies on subtropical mode
744 water variability from the Kuroshio Extension System Study (KESS). *Journal of*
745 *Physical Oceanography*, 37(4), 982-1000.
- 746 Qiu, B., & Chen, S., 2010. Eddy-mean flow interaction in the decadal modulating
747 Kuroshio Extension system. *Deep Sea Research Part II: Topical Studies in*
748 *Oceanography*, 57(13-14), 1098-1110.



- 749 Qu, T., Xie, S.P., Mitsudera, H. and Ishida, A., 2002. Subduction of the North Pacific
750 mode waters in a global high-resolution GCM. *Journal of physical oceanography*,
751 32(3), 746-763.
- 752 Qu, T. and Chen, J., 2009. A North Pacific decadal variability in subduction rate.
753 *Geophysical Research Letters*, 36(22), L22602.
- 754 Resplandy, L., Lévy, M. and Mcgillicuddy, D.J., 2019. Effects of eddy-driven
755 subduction on ocean biological carbon pump. *Global Biogeochemical Cycles*, 33(8),
756 pp.1071-1084.
- 757 Robinson, C., 2019. Microbial respiration, the engine of ocean deoxygenation.
758 *Frontiers in Marine Science*, 5, 533.
- 759 Sabine, C.L., Feely, R.A., Gruber, N., Key, R.M., Lee, K., Bullister, J.L., Wanninkhof,
760 R., Wong, C.S.L., Wallace, D.W., Tilbrook, B. and Millero, F.J., 2004. The oceanic
761 sink for anthropogenic CO₂. *Science*, 305(5682), 367-371.
- 762 Sarmiento, J.L., & Gruber, N., 2006. *Ocean biogeochemical dynamics*. Princeton
763 University Press.
- 764 Siegel, D. A., Buesseler, K. O., Doney, S. C., Sailley, S. F., Behrenfeld, M. J., & Boyd,
765 P. W., 2014. Global assessment of ocean carbon export by combining satellite
766 observations and foodassessment of *Global Biogeochemical Cycles*, 28(3), 181-196.
- 767 Steinberg, D. K., Van Mooy, B. A., Buesseler, K. O., Boyd, P. W., Kobari, T., & Karl,
768 D. M., 2008. Bacterial vs. zooplankton control of sinking particle flux in the ocean's
769 twilight zone. *Limnology and Oceanography*, 53(4), 1327-1338.
- 770 Stramma, L., Johnson, G. C., Sprintall, J., & Mohrholz, V., 2008. Expanding oxygen-
771 minimum zones in the tropical oceans. *science*, 320(5876), 655-658.
- 772 Stukel, M.R., Aluwihare, L.I., Barbeau, K.A., Chekalyuk, A.M., Goericke, R., Miller,
773 A.J., Ohman, M.D., Ruacho, A., Song, H., Stephens, B.M. and Landry, M.R., 2017.
774 Mesoscale ocean fronts enhance carbon export due to gravitational sinking and
775 subduction. *Proceedings of the National Academy of Sciences of the United States*
776 *of America*, 114(6), 1252-1257.
- 777 Stukel, M.R., Song, H., Goericke, R. and Miller, A.J., 2018. The role of subduction and
778 gravitational sinking in particle export, carbon sequestration, and the
779 remineralization length scale in the California Current Ecosystem. *Limnology and*
780 *Oceanography*, 63(1), 363-383.
- 781 Takano, Y., Ito, T., & Deutsch, C., 2018. Projected centennial oxygen trends and their
782 attribution to distinct ocean climate forcings. *Global Biogeochemical Cycles*, 32(9),
783 1329-1349.
- 784 Talley, L. D., 1997. North Pacific Intermediate Water transports in the mixed water
785 region. *Journal of physical oceanography*, 27(8), 1795-1803.
- 786 Williams, R.G., 2001. Ocean Subduction, in: *Encyclopedia of Ocean Sciences*. Elsevier,
787 pp. 1982-1993.
- 788 Wohlers, J., Engel, A., Zöllner, E., Breithaupt, P., Jürgens, K., Hoppe, H. G., ... &
789 Riebesell, U., 2009. Changes in biogenic carbon flow in response to sea surface
790 warming. *Proceedings of the national academy of sciences*, 106(17), 7067-7072.



- 791 Xu, L., Xie, S.P., McClean, J.L., Liu, Q. and Sasaki, H., 2014. Mesoscale eddy effects
792 on the subduction of North Pacific mode waters. *Journal of Geophysical Research:*
793 *Oceans*, 119(8), 4867-4886.
- 794 Xu, L., Li, P., Xie, S.P., Liu, Q., Liu, C. and Gao, W., 2016. Observing mesoscale eddy
795 effects on mode-water subduction and transport in the North Pacific. *Nature*
796 *communications*, 7, 10505.
- 797 Yasuda, I., Okuda, K., & Shimizu, Y., 1996. Distribution and modification of North
798 Pacific Intermediate Water in the Kuroshio-Oyashio interfrontal zone. *Journal of*
799 *physical oceanography*, 26(4), 448-465.
- 800 Zhang, Z., Wang, W., & Qiu, B., 2014. Oceanic mass transport by mesoscale eddies.
801 *Science*, 345(6194), 322-324.
- 802 Zhang, Z., Li, P., Xu, L., Li, C., Zhao, W., Tian, J., & Qu, T. (2015). Subthermocline
803 eddies observed by rapid-sampling Argo floats in the subtropical northwestern
804 Pacific Ocean in Spring 2014. *Geophysical Research Letters*, 42(15), 6438-6445.
- 805 Zhang, Y., Zhang, Z., Chen, D., Qiu, B., & Wang, W., 2020. Strengthening of the
806 Kuroshio current by intensifying tropical cyclones. *Science*, 368(6494), 988-993.
- 807 Zhu, R., Chen, Z., Zhang, Z., Yang, H., & Wu, L., 2021. Subthermocline eddies in the
808 Kuroshio Extension region observed by mooring arrays. *Journal of Physical*
809 *Oceanography*, 51(2), 439-455.